J Mater Sci (2012) 47:8360–8366
DOI 10.1007/s10853-012-6660-3

HTC 2012

Phase separation in monotectic alloys as a route for liquid state fabrication of composite materials

I. Kaban · M. Köhler · L. Ratke · R. Nowak · N. Sobczak · N. Mattern · J. Eckert · A. L. Greer · S. W. Sohn · D. H. Kim

Received: 20 April 2012 / Accepted: 10 June 2012 / Published online: 30 June 2012

Abstract The mechanism of liquid–liquid phase separation and factors determining the solid-state microstructure of monotectic alloys are discussed. The effect of the cooling rate on the phase-separated morphology is shown in examples of Al–In, Al–Pb, Ni–Nb–Y and Zr–Gd–Co–Al alloys solidified by different techniques. A remarkable improvement of the microstructure for the $Al_{91}Pb_9$ hypermonotectic alloy cast with TiB_2 particles, which catalyze the phase separation, is demonstrated.

I. Kaban (✉) · N. Mattern · J. Eckert
IFW Dresden, Institute for Complex Materials, P.O. Box 270116, 01171 Dresden, Germany
e-mail: i.kaban@ifw-dresden.de

M. Köhler · L. Ratke
Institut für Materialphysik im Weltraum, Deutsches Zentrum für Luft- und Raumfahrt (DLR), 51170 Köln, Germany

R. Nowak · N. Sobczak
Center for High-Temperature Studies, Foundry Research Institute, Zakopianska Str. 73, 30-418 Cracow, Poland

J. Eckert
TU Dresden, Institute of Materials Science, 01062 Dresden, Germany

A. L. Greer
Department of Materials Science & Metallurgy, University of Cambridge, Pembroke Street, Cambridge CB2 3QZ, UK

S. W. Sohn · D. H. Kim
Department of Metallurgical Engineering, Center for Noncrystalline Materials, Yonsei University, Seoul 120-749, Korea

Liquid phase separation in hypermonotectic alloys

Multicomponent alloys with a miscibility gap in the liquid state, so-called *monotectic* alloys, are a focus of fundamental and applied research into the design of new composites. Combining different phases can generate novel materials with exceptional functional properties quite unlike those of each phase taken separately. The properties of nano- and microphase-separated alloys can be very different, as is evident in cases such as glass colouring, optical nonlinearity, superionic conductivity, enhanced magnetoresistance, increased toughness, improved plasticity, reduced wear friction, etc. The required properties can be tailored by tuning the volume fractions of coexisting phases, their size, and their spatial distribution. In the following, we discuss the mechanisms of liquid–liquid phase separation, factors determining the solid-state morphology of monotectic alloys, and liquid state fabrication of composite materials using methods that exploit phase separation.

A schematic phase diagram of a binary system with miscibility gap is shown in Fig. 1. The composition and temperature region where the miscibility–immiscibility transition occurs are bounded by the coexistence (*binodal*) line, the locus of temperatures T_{bin} [1–3]. Above the coexistence curve, the two components are completely miscible and only one phase exists. Below the coexistence curve, the single-phase is metastable, and the equilibrium state of the system has two liquid phases of different chemical composition. Below the *spinodal* line, the system is unstable. In the metastable region, phase separation proceeds by nucleation and growth of the liquid minority-phase, characterized by large-amplitude chemical fluctuations over a small spatial extent, generally leading to a droplet morphology [1–5]. In the unstable region, the phase transition occurs by a spinodal

mechanism, characterized by long-range fluctuations, initially of very small amplitude, yielding an interconnected phase-separated structure [1–3].

If a homogeneous single-phase liquid L of solute content $x > x_M$ (Fig. 1) is cooled from a temperature T_0 above the binodal line to a temperature T_1 in the metastable region or to a temperature T_2 in the unstable region it demixes into the liquids L_1 and L_2. At the monotectic temperature T_M, the liquid L_1 decomposes into a solid phase S_1 and the liquid phase L_2. Upon further cooling, the composition of the liquid L_2 changes along the liquidus line to x_E and it solidifies at the temperature T_E in a terminal eutectic reaction $L_2 \rightarrow S_1 + S_2$.

As concentration fluctuations at the binodal temperature T_{bin} are energetically unfavourable, undercooling of the melt below T_{bin} is required to nucleate the L_2-liquid phase. The undercooling $\Delta T = T - T_{bin}$ depends on the alloy system as well as on the alloy composition. Near the critical point (x_C, T_C), the two coexisting phases are nearly identical and the energy barrier for the nucleation is very low; therefore demixing occurs at millidegrees undercooling of T_C [6]. ΔT increases by moving from the critical concentration to the monotectic concentration [7–9]. Depending on the system, the undercooling may reach various values from a few to several tens of degrees (K) for hypermonotectic alloys close to x_M as has been shown experimentally [8, 9]. The nucleated droplets of L_2-liquid are embedded in a highly saturated matrix and grow by diffusive transport of the solute in the matrix. In order to produce composites with finely dispersed minority-phase particles in a majority-phase matrix from hypermonotectic alloys, one has to be able to control the size and distribution of the

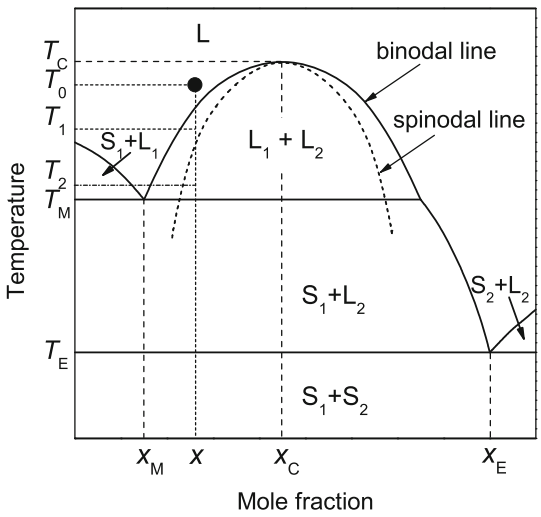

Fig. 1 Schematic phase diagram of a binary system with liquid–liquid miscibility gap. T_C is the critical, T_M is the monotectic, and T_E is the eutectic temperature; x_M is the monotectic and x_E is the eutectic composition

L_2-droplets in the L_1-matrix before and during solidification. For this, different physical properties and processes need to be considered.

Factors determining the solid-state morphology

The solid-state morphology of hypermonotectic alloys demixed in the metastable region is essentially the result of the interplay between the growth and motion of L_2-phase droplets. Principally, the growth of L_2-droplets embedded in a supersaturated L_1-matrix depends on the effective diffusion coefficient D, the time elapsed t, and the relation of solute concentrations in the matrix liquid C_{matr}, in the L_2-droplet C_{drop}, and at the matrix/droplet interface C_{interf} [4, 5]:

$$R = \sqrt{D\frac{C_{matr} - C_{interf}}{C_{drop} - C_{interf}}}\sqrt{t}. \quad (1)$$

According to Eq. (1), the droplet radius R decreases with increasing cooling rate proportionally to $(dT/dt)^{-1/2}$.

Also, the droplets grow due to Ostwald ripening (growth of larger drops at the expense of smaller droplets) and coalescence caused from collisions of the moving droplets [10, 11]. The movement of droplets in the liquid matrix is mainly determined by four processes: Brownian motion, Stokes sedimentation, Marangoni (thermocapillary) motion, and matrix convection [4, 11, 12]. The Brownian motion is appreciable for the droplets with radius less than 1 μm, while the effects of Stokes sedimentation and Marangoni motion become significant with increasing droplet size. The terminal settling velocity v_S due to gravity is determined by the difference in densities of the droplet and of the liquid matrix ($\rho_{drop} - \rho_{matr}$), their viscosities ($\eta_{drop}$ and η_{matr}), and the droplet radius R [5]

$$v_S = \frac{2\,g\,(\rho_{drop} - \rho_{matr})}{3}\frac{\eta_{matr} + \eta_{drop}}{\eta_{matr}(2\eta_{matr} + 3\eta_{drop})}R^2, \quad (2)$$

where g is the gravitational acceleration. The Marangoni velocity v_M is determined by the droplet radius R, the viscosity of the matrix and of the droplet, their thermal conductivities λ_{matr} and λ_{drop}, and the temperature dependence of the interfacial tension σ between the coexisting liquids [5]

$$v_M = -\frac{2R}{\left[\left(2\lambda_{matr} + \lambda_{drop}\right)/\lambda_{matr}\right]\left(2\eta_{matr} + 3\eta_{drop}\right)}\frac{\partial\sigma}{\partial T}\nabla T, \quad (3)$$

where ∇T is the temperature gradient in the molten alloy.

In general, the microstructure of a solid alloy showing immiscibility in the liquid state is determined by its thermophysical properties and casting conditions. This suggests that variation in the processing temperature and

cooling rate is a tool for controlling the size and spatial distribution of coexistent phases. The nucleation rate for L_2-liquid would increase at higher undercooling below the binodal temperature. As a reduction in temperature results in a decrease of atomic mobility, decreasing the solidification temperature would reduce the diffusion-controlled minority-phase growth rate and thermocapillary motion, as well as Ostwald ripening and coalescence. Finally, increasing cooling rate facilitates rapid trapping of minority-phase particles in the matrix.

Solidification of hypermonotectic alloys under different conditions

Experimental procedures

Al–In and Al–Pb master alloys were produced by melting of high-purity Al, In and Pb (99.99+ %) in graphite crucibles. Ni–Nb–Y and Zr–Gd–Co–Al master alloys were prepared by arc-melting of high-purity components (99.9+ %) in a Ti-gettered Ar atmosphere in a water-cooled Cu crucible.

$Al_{92}In_8$ and $Al_{64}In_{36}$ alloys (wt%) were solidified in a device for high-temperature investigations described elsewhere [13]. The vertical resistance-heating furnace was evacuated to a vacuum of about 1×10^{-6} mbar and filled with argon to a total pressure of ~ 1 bar. The samples were heated in graphite capillaries (6 mm in diameter) at a rate of about 0.15 K s^{-1} up to 900 °C and kept there for 10 min. Then a small drop was squeezed from the capillary onto an Al_2O_3 substrate and the system was cooled down through the miscibility gap at a rate of about 0.25 K s^{-1}.

$Ni_{54}Nb_{23}Y_{23}$ alloy (at.%) was rapidly quenched by the melt-spinning on a copper wheel under Ar atmosphere. Ribbons of about 3-mm width and 30-μm thickness were obtained. Quenching at a lower cooling rate has been carried out with electromagnetically levitated $Ni_{54}Nb_{23}Y_{23}$ drops of about 6 mm diameter. After falling onto a copper plate, discs of about 12-mm diameter and 1-mm thickness were produced. In both cases, the Ni–Nb–Y liquid alloy was heated by an induction coil up to about 1500 °C before quenching.

$Zr_{35}Gd_{23}Co_{23}Al_{19}$ alloy (at.%) was re-melted in a quartz tube and injection-cast into a water-cooled copper mould with an inner bore of 1-mm diameter and 20-mm length.

The mould-casting of the $Al_{91}Pb_9$ (wt%) alloys was carried out with and without inoculant. The samples were heated under Ar atmosphere up to 1050 °C and kept for 60 min to ensure homogenization. The inoculant (TiB_2 powder, <4 μm, ESK Ceramics) already mixed with lead powder and compacted was added to the Al–Pb molten alloy 5 min before casting and the alloy was stirred to disperse the particles in the volume and avoid their settling. The alloys were finally cast into a steel mould with a bore of 12-mm inner diameter and 60-mm length. After solidification, pieces from the middle of the samples were cut out for the microstructure analysis.

An $Al_{91}Pb_9$ (wt%) ingot cast in a steel mould was used for rapid quenching. The alloy was heated to about 1100 °C and held for 2 min before melt-spinning on a copper wheel under Ar atmosphere. Ribbons of about 5-mm width and 80-μm thickness were obtained.

The cross-sections of the solidified samples were investigated with scanning electron microscopy (SEM) combined with energy-dispersive X-ray (EDX) spectrometry (LEO GEMINI 1530 and JEOL JSM-7100F). Three-dimensional images of the Al–In and Al–Pb samples were obtained with X-ray computed tomography (Phoenix nanotom).

Slow cooling

Slow cooling of hypermonotectic melts from a single-phase state into a liquid–liquid miscibility gap results in phase separation via a nucleation and growth mechanism. The size and spatial distribution of coexisting phases in the solidified alloys depend on the factors described above, on the relative volume fractions of the phases, as well as on the balance of interfacial energies and wetting of the phases [14]. For example, all of the three Al–In alloys cooled at about 0.25 K s^{-1} in the same furnace showed very distinct macro-phase separation, as demonstrated in Figs. 2, 3. However, the spatial distribution of the Al-rich and In-rich phases is quite different. The $Al_{64}In_{36}$ (at.%) alloy in a graphite container solidified with one layer on top of another (Fig. 2). If a drop of the same alloy was squeezed from the container onto an Al_2O_3 substrate, then the Al-rich phase has formed a large droplet at the middle-top of the sample as shown in the 3D-view in Fig. 3a. The phase-separated morphology of the indium-poor sample on the Al_2O_3 substrate (Fig. 3b) is different. There is just a small droplet at the top of the $Al_{92}In_8$ (at.%) alloy and irregularly distributed In-rich particles at the sample surface.

Fast cooling

Phase separation has been known for a long time to occur in multicomponent metal-oxide and chalcogenide glasses [1, 2, 15–17]. The excellent glass-forming ability of metal-oxide liquids such as silicates, borates, phosphates etc., or their combinations, is related to the high viscosity in the liquid and the supercooled-liquid state, which impedes nucleation and crystal growth upon cooling into the solid-state. Low atomic diffusivity has a crucial impact not only on the crystallization, but also on the phase separation in the liquid state. Upon fast cooling of metal-oxide mixtures,

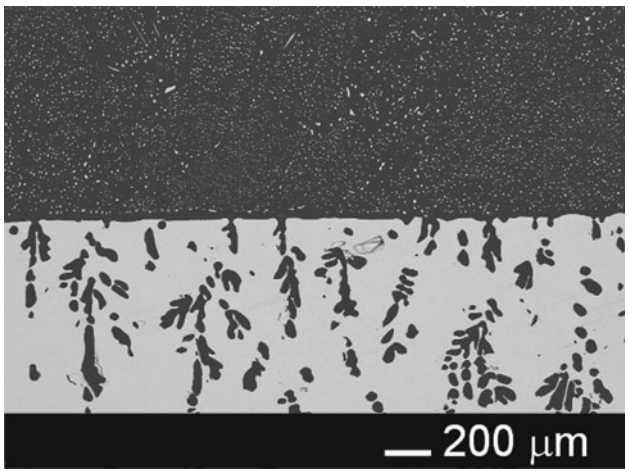

Fig. 2 $Al_{64}In_{36}$ (at.%) alloy solidified at about 0.25 K s^{-1} in a graphite container: SEM image taken at the interface between the Al-rich (*dark*) and In-rich (*light*) phases

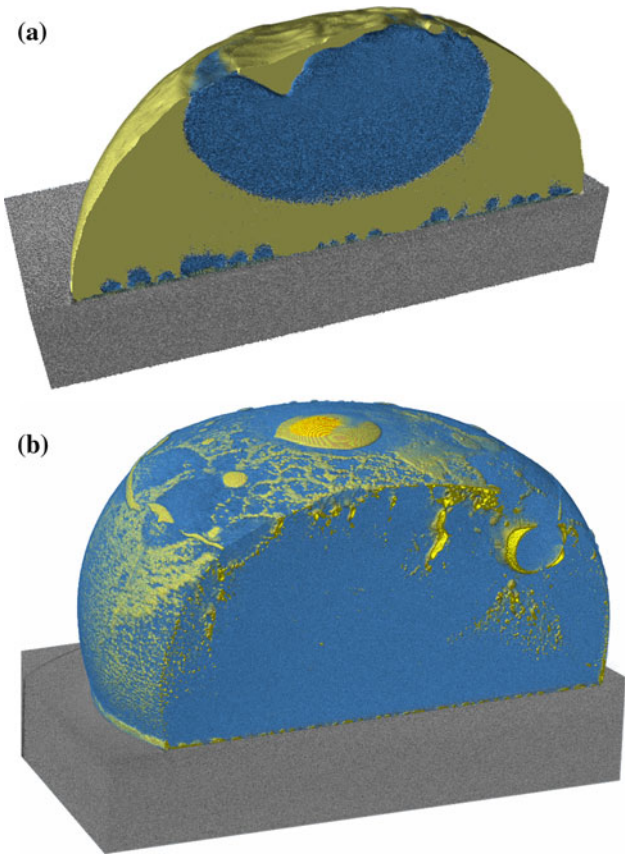

Fig. 3 (Colour online) X-ray tomography images of **a** $Al_{64}In_{36}$ and **b** $Al_{92}In_8$ alloys (at.%) solidified at about 0.25 K s^{-1} on Al_2O_3 substrates: *dark* (*blue*) phase—Al-rich; *light* (*yellow*) phase—In-rich

it is relatively easy to pass through the metastable region without phase separation, which then occurs in the unstable (spinodal) region [1]. In favourable cases, the phase separation can be suppressed completely by increased cooling rate. It can be triggered or enhanced by subsequent heat treatment of a homogeneous or nanophase-separated glassy alloy. Also, by proper selection of alloy composition and cooling rate, multiple phase separations with formation of different phases can be achieved.

Recently, phase-separated metallic glasses have been fabricated by rapid quenching of multicomponent metallic melts exhibiting good glass-forming ability and liquid–liquid immiscibility [18–22]. Rapid quenching can be realized by several methods, among which the melt-spinning is the most widely used. In melt-spinning, a jet of a molten alloy impinges on the surface of a rotating copper wheel, yielding a continuous solid ribbon, and giving cooling rates of 10^5–10^6 K s^{-1}. A cooling rate of 10^2–10^3 K s^{-1} is typical for the quenching of a liquid alloy drop freely falling onto a metallic chill plate. In both methods, the cooling rate varies strongly across the sample.

Figure 4 shows scanning electron microscope images of cross-sections for the phase-separated $Ni_{54}Nb_{23}Y_{23}$ (at.%) alloy rapidly quenched by the two different methods from a liquid initially heated to the same temperature (1500 °C): Fig. 4a—ribbon obtained by melt-spinning, Fig. 4b—flattened drop obtained by free fall onto a copper plate. The size of minority-phase (NiNb-rich) particles is about 10^2 times larger in the copper plate-quenched sample than in the melt-spun ribbon, due to the very different cooling rates. The large difference in the cooling rate for the two methods is also indicated by the fact that both solid phases are amorphous in the melt-spun ribbon, while they are crystalline in the copper plate-quenched drop, as proven by X-ray diffraction (not shown). The size of minority-phase particles varies remarkably between the copper-contact side and the free ribbon surface due to the gradients in temperature and cooling rate in this direction. As the liquid–liquid interfacial tension σ decreases with increasing temperature according to the power law $(1 - T/T_C)^{\beta}$ with the exponent β close to 1.3 [23–26], the temperature gradient causes thermocapillary motion of the nucleated minority-phase droplets from the cold copper-side to the warmer contact-free surface; the droplets then coalesce and grow.

It has been demonstrated recently that binodal-type phase separation can be overcome in glass-forming metallic alloys with a liquid miscibility gap if T_{bin} is close to the glass-transition temperature [19, 22]. The size of minority-phase particles has been determined to be 2–5 nm in a melt-spun $Cu_{50}Zr_{45}Gd_5$ amorphous alloy [22]. Nanoscale phase separation of spinodal-type has been achieved in an injection-cast $Zr_{28}Y_{28}Al_{22}Co_{22}$ bulk metallic glass in the work [19]. Figure 5 shows the SEM image taken close to the surface of the $Zr_{35}Gd_{23}Co_{23}Al_{19}$ glassy rod (about 50 μm from the edge). The average composition of the light phase is $Zr_{17}Gd_{43}Al_{30}Co_{10}$ (at.%) and that of the dark

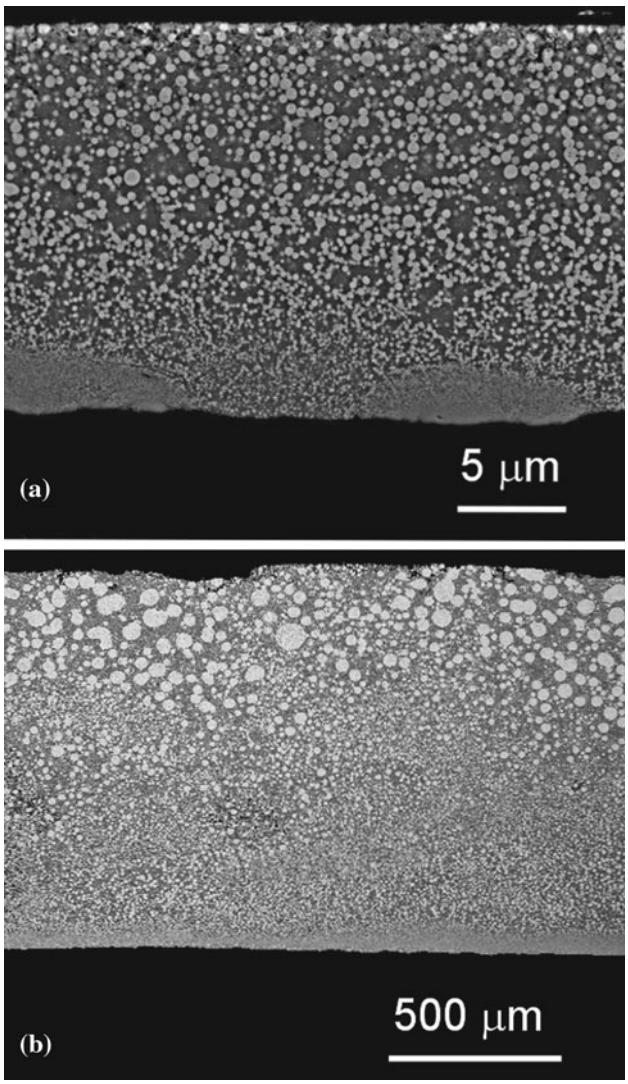

Fig. 4 SEM micrographs of $Ni_{54}Nb_{23}Y_{23}$ (at.%) alloy quenched by melt-spinning (**a**) and by dropping of a liquid droplet onto a copper plate (**b**). Bottom of the images corresponds to the copper-contact side. *Light* phase—NiNb-rich, *dark* phase—NiY-rich. Please note that the image scales differ by two orders of magnitude

phase is $Zr_{45}Gd_9Al_{20}Co_{26}$ (at.%) as determined by the EDX spectroscopy. The observed phase-separated morphology is very similar to a "worm-like" structure typical for decomposition via a spinodal mechanism.

The SEM image taken at the middle of a cross-sectioned $Al_{91}Pb_9$ (wt%) ribbon obtained by melt-spinning is shown in Fig. 6 along with the SEM image taken at the middle of a cross-sectioned $Al_{91}Pb_9$ (wt%) rod cast in a steel mould. The size of minority-phase (Pb-rich) particles formed through the binodal phase separation differs by more than 10^2 times for these two methods. It varies between 100 and 300 nm in the melt-spun ribbon (Fig. 6a) and from some micrometres to some tens of micrometres in the mould-cast

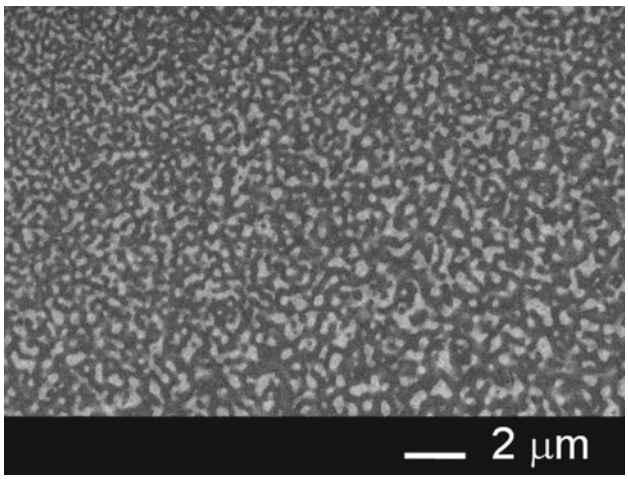

Fig. 5 SEM image taken at the edge region (50 μm inside) of the injection-cast $Zr_{35}Gd_{23}Co_{23}Al_{19}$ rod (at.%). *Light* phase—GdAl-rich, *dark* phase—ZrCo-rich

sample (Fig. 6b). In both cases, there are a number of small particles formed at the boundaries of α-Al grains through the monotectic reaction. The reason for this might be either relatively large supercooling of the $Al_{91}Pb_9$ melt by the melt-spinning and/or a high supersaturation of the Al-matrix by mould-casting.

Moderate cooling

It is widely accepted that the phase separation of a hypermonotectic melt in the metastable region starts by homogeneous nucleation. However, studies of grain refining in Al-based monotectic alloys upon addition of inoculants revealed that they have affected not just the matrix microstructure, but also the minority-phase [27, 28], which indicates heterogeneous nucleation of the L_2-liquid. In the framework of classical theory [2, 29, 30], the minority-phase L_2 can nucleate heterogeneously on the inoculant particles if they are preferably wetted by the liquid L_2 in the presence of the liquid L_1. The contact angle θ at the triple line *inoculant*/L_1/L_2 determines the relative nucleation barrier $f(\theta)$ for nucleation, so-called catalytic factor [2, 29, 30]:

$$f(\theta) = \frac{\Delta G_{\text{het}}}{\Delta G_{\text{hom}}} = \frac{(2+\cos\theta)(1-\cos\theta)^2}{4}, \tag{4}$$

where ΔG_{het} is the energy barrier for heterogeneous nucleation. ΔG_{hom} is the energy barrier for homogeneous nucleation

$$\Delta G_{\text{hom}} = \frac{16\pi}{3}\frac{\sigma^3}{\Delta G_{\text{V}}^2}, \tag{5}$$

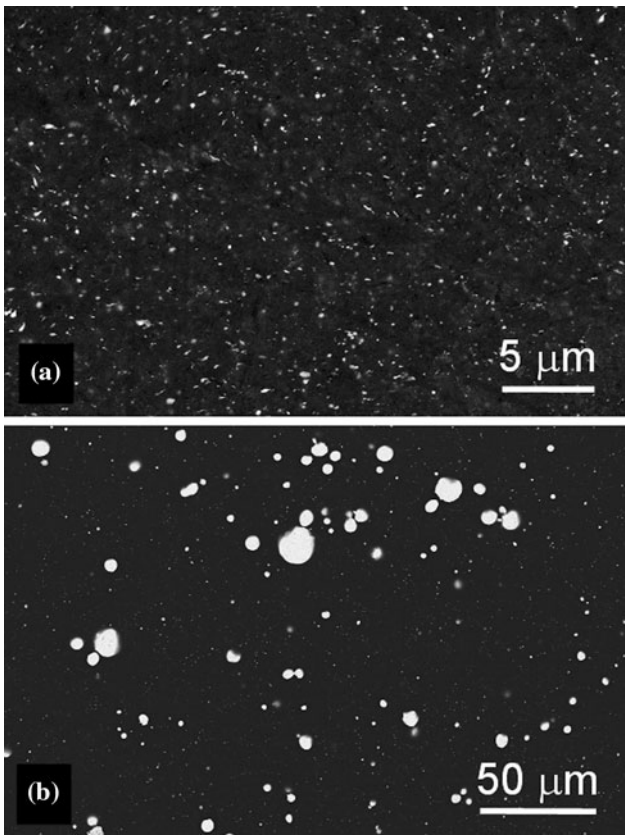

Fig. 6 SEM images taken at the middle of melt-spun (**a**) and mould-cast (**b**) $Al_{91}Pb_9$ (wt%) alloys. Please note that the image scales differ by one order of magnitude

where σ is the interfacial tension between liquids L_1 and L_2; ΔG_V is the Gibbs free energy change per unit volume associated with the formation of the L_2-phase.

Hence, the nucleation rate I of liquid phase L_2 in an immiscible alloy (Eq. 6) can be greatly enhanced by addition of properly selected inoculant particles [2, 29, 30]:

$$I = I_0 \exp\left(-\frac{\Delta G_{\text{hom}} f(\theta)}{kT}\right), \tag{6}$$

where I_0 is a pre-exponential factor, k is the Boltzmann constant and T is the absolute temperature.

Measurements of the wetting angle for Al_2O_3, ZrO_2 and TiB_2 ceramics at the liquid–liquid interface in Al–Bi, Al–In and Al–Pb monotectic alloys [26, 31] suggest that all of these ceramics have the potential to catalyse nucleation of the liquid phase L_2. The best results for the $Al_{91}Pb_9$ (wt%) hypermonotectic alloy have been obtained in casting experiments with addition of TiB_2 particles [26, 32]. As an example, three-dimensional images taken at the centre of the $Al_{91}Pb_9$ ingots cast with and without TiB_2 inoculant are shown in Fig. 7. The size and spatial distribution of the Pb-particles in the Al-matrix of the reference TiB_2-free alloy are remarkably non-uniform (Fig. 7a). On the other hand, Pb-particles of notably smaller size are regularly distributed in the ingot cast with TiB_2 particles (Fig. 7b). The size-number distribution plot in Fig. 8 clearly demonstrates that the addition of the inoculant results in a significant increase in the number of Pb-particles and in a decrease of their size. Obviously, the number of nucleated L_2-droplets is markedly increased by addition of TiB_2 inoculant. As the L_2-phase is distributed over a large number of nucleated droplets, the supersaturation of Al-rich matrix is reduced; thus, there is less Pb for particle growth. The smaller the particles, the smaller are the side-effects affecting their growth.

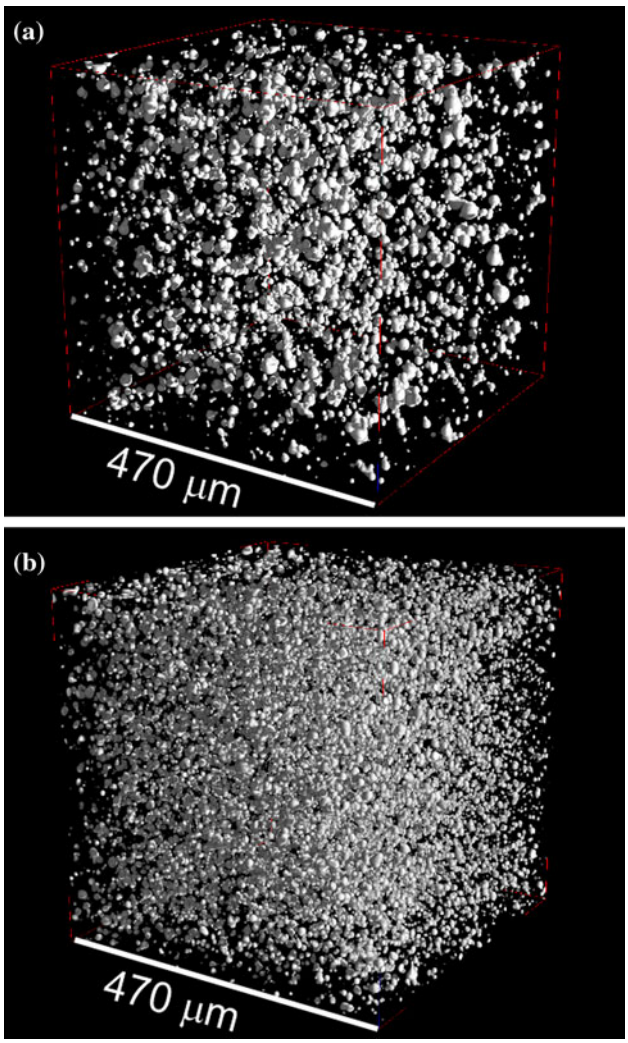

Fig. 7 Three-dimensional images (X-ray computed tomography) of $Al_{91}Pb_9$ (wt%) alloys cast without inoculant (**a**) and with 1.0 wt% of TiB_2 inoculant (**b**). The Al-based matrix has been made transparent for better presentation of the Pb-rich particles

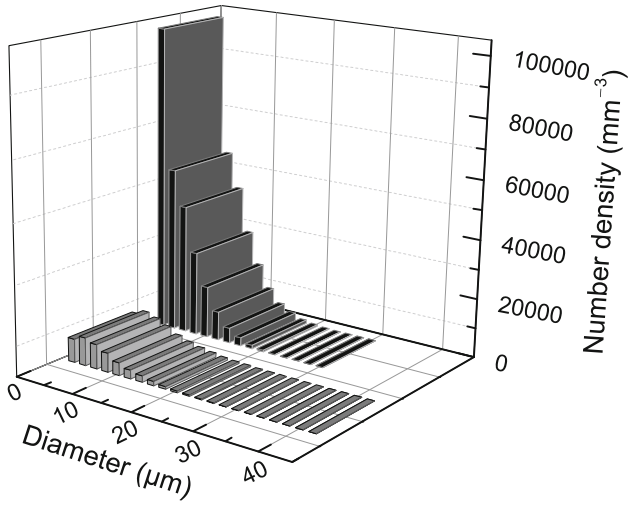

Fig. 8 Size-number distribution of Pb-rich particles in the $Al_{91}Pb_9$ (wt%) alloys, estimated from the 3D-images: cast without inoculant (*grey*) and with 1.0 wt% of TiB_2 inoculant (*black*)

Summary

Composites made of multicomponent alloys with liquid–liquid miscibility are the focus of basic and applied research on design of new materials with exceptional functional properties. The solid-state microstructure of monotectic alloys is essentially determined by their thermophysical properties and solidification parameters. While the liquid state fabrication of phase-separated metal-oxide glasses with fine and tunable microstructure has been well established, it is still under development for metallic alloys. One of the methods for obtaining solid hypermonotectic alloys with fine microstructure is rapid quenching. Casting of liquid alloys with a miscibility gap, adding inoculants to achieve heterogeneous nucleation of the minority liquid phase, have been shown to offer a new possibility for fabrication of composite materials with a remarkably uniform dispersion of minority-phase in the matrix.

Acknowledgements This study has partly been funded by the German Research Foundation DFG (Contracts No. Ka-3209/1-2, Ra-537/10). The Foundry Research Institute Cracow and the Global Research Laboratory Program of the Korean Ministry of Education, Science and Technology are acknowledged for the support of this study. O. Shuleshova is acknowledged for helpful discussions. B. Korpała, G. Bruzda and A. Tchorz are thanked for technical assistance.

References

1. Vogel W (1979) Glasschemie. VEB Deutscher Verlag für Grundstoffindustrie, Leipzig
2. Kelton KF, Greer AL (2010) Nucleation in condensed matter: applications in materials and biology. Elsevier (Pergamon Materials Series), Amsterdam
3. Cahn JW (1968) Trans Metall Soc AIME 242:166
4. Zhao JZ, Ratke L, Feuerbacher B (1998) Model Simul Mater Sci Eng 6:123
5. Zhao J, Ratke L, Jia J, Li Q (2002) J Mater Sci Technol 18:197
6. Greer SC (1978) Acc Chem Res 11:427
7. Cahn JW (1969) J Am Chem Soc 52:118
8. Perepezko JH, Galaup C, Cooper KP (1982) In: Rindone GE (ed) Materials processing in reduced gravity environment of space. Elsevier, Amsterdam, p 491
9. Uebber N, Ratke L (1991) Scr Metall Mater 25:1133
10. Ratke L, Thieringer WK (1985) Acta Metall 33:1793
11. Ratke L (1987) J Colloid Interface Sci 119:391
12. Wu M, Ludwig A, Ratke L (2003) Metall Mater Trans A 34:3009
13. Sobczak N, Nowak R, Radziwill W, Budzioch J, Glenz A (2008) Mater Sci Eng A 495:43
14. Chatain D, Wynblatt P, de Ruijter M, de Conninck J, Carter C (1999) Acta Mater 47:3049
15. Porai-Koshits EA, Averjanov VI (1968) J Non-Cryst Solids 1:29
16. Uhlmann DR, Kolbeck AG (1976) Phys Chem Glasses 17:146
17. Andrikopoulos KS, Arvanitidis J, Dracopoulos V, Christofilos D, Wagner T, Yannopoulos SN (2011) Appl Phys Lett 99:171911
18. Kündig AA, Ohnuma M, Ping DH, Ohkubo T, Hono K (2004) Acta Mater 52:2441
19. Park BJ, Chang HJ, Kim DH, Kim WT, Chattopadhyay K, Abinandanan TA, Bhattacharyya (2006) Phys Rev Lett 96:245503
20. Mattern N, Kühn U, Gebert A, Gemming T, Zinkevich M, Wendrock H, Schultz L (2005) Scr Mater 53:271
21. Han JH, Mattern N, Kim DH, Eckert J (2011) J Alloy Compd 509S:S42
22. Mattern N, Shariq A, Schwarz B, Vainio U, Eckert J (2012) Acta Mater 60:1946
23. Rowlinson SS, Widom B (1982) Molecular theory of capillarity. Clarendon Press, Oxford
24. Kaban IG, Hoyer W (2008) Phys Rev B 77:125426
25. Kaban I, Curiotto S, Chatain D, Hoyer W (2010) Acta Mater 58:3406
26. Kaban I, Köhler M, Ratke L, Hoyer W, Mattern N, Eckert J, Greer AL (2011) Acta Mater 59:6880
27. Moiseev J, Zak H, Palkowski H, Tonn B (2005) Aluminium 81:92
28. Ratke L, Brück S, Mathiesen R, Ludwig A, Gruber-Pretzler M, Tonn B, Gzovskyy K, Gránásy L, Tegze G, Ågren J, Hoglund L, Arnberg L, Gust E, Anger G, Lauer M, Garen R, Reifenhäuser B (2007) Trans Indian Inst Metals 60:103
29. Turnbull D (1950) J Appl Phys 21:1022
30. Greer AL (2010) Scr Mater 62:899
31. Kaban I, Köhler M, Hoyer W, Ratke L (2010) High Temp High Press 39:347
32. Köhler M, Ratke L, Kaban I, Hoyer W (2011) IOP Conf Ser Mater Sci Eng 27:012005